

RESEARCH

Open Access



Heat recovery optimization of a shell and tube bundle heat exchanger with continuous helical baffles for air ventilation systems

Md Ashfaquul Bari^{1*} , Manuel Münsch^{1*}, Bastian Schöneberger¹, Bernhard Schlagbauer¹, Andrea Alina Tiu¹ and Andreas Wierschem¹

Abstract

We report a numerical evaluation of the impact of continuous helical baffle on the heat recovery efficiency of counterflow tube bundle heat exchangers. The baffle inclination angle has been varied from 11° to 22°. Since the fluid flows over the tube bundle at an angle due to helical flow inside the shell, the heat exchanger operates in cross counter mode. Fluent simulations with the $k-\omega$ transition shear stress transport turbulence model have been performed to investigate the thermal-hydraulic parameters of the system in terms of heat recovery efficiency, pressure loss, and overall heat transfer rate. Outside air temperature has been varied to mimic cold and warm weather. Pressure loss has been constrained to be less than 250 Pa, conforming to EU guidelines for energy labeling of residential ventilation units. At the maximum volume flow rate of 40 m³/h, the device performed with over 80% heat recovery efficiency for the considered temperature difference. Continuous helical baffles helped to improve convective heat transfer by reducing cross flow area and increasing velocity. Smaller angles result in greater pressure loss while having no discernible effect on heat recovery efficiency for the considered geometry. The analysis demonstrates the potential of a compact counterflowing recuperative heat exchanger with continuous helical baffles for decentralized ventilation systems and serves as a basis for further optimization.

Keywords Continuous helical baffle, Compact recuperative heat exchangers, Cross-counter flow, Decentralized ventilation, Air to air heat exchanger, $k - \omega$ transition SST, Grid Convergence Index (GCI)

1 Introduction

Air handling units (AHU) are widely used in commercial, food processing, manufacturing, and residential buildings to maintain air quality indoors. To maintain the air quality inside an enclosed space, AHUs need to run

continuously and in turn increase energy requirements to maintain optimal temperature indoors. To circumvent this, AHU with integrated air-to-air heat recovery systems are used. On the other hand, buildings in the European Union (EU) have to be by default airtight to maintain higher energy efficiency standards [1]. Airtight buildings without any air exchangers have a higher susceptibility to mold formation from trapped humidity. In the EU, around 75% of buildings are not energy efficient and are responsible for approximately 40% of the total energy consumption, of which 85% is spent on heating and hot water [2]. Energy-efficient buildings are a must have according to the European Green Deal [3].

*Correspondence:

Md Ashfaquul Bari
md.ashfaquul.bari@fau.de; md.ashfaquul.bari@gmail.com

Manuel Münsch
manuel.muensch@fau.de

¹ Friedrich-Alexander Universität Erlangen-Nürnberg (FAU), Lehrstuhl für Strömungsmechanik (LSTM), Cauerstraße 4, Erlangen 91058, Germany



In Germany, bulk of the heating is generated by either burning natural gas (47.2%) or oil (25.6%) and at the end of year 2021 about 16.2% was supplied by renewable energy [4]. The development of energy-efficient systems is of absolute importance to tackle the challenge of climate change. In principle, integrating a recuperative heat exchanger parallel to fine dust filtering in a ventilation system has the potential for significant energy efficiency improvements.

Tube bundle heat exchangers are frequently used due to their high flexibility, easy maintenance and cost efficiency [5, 6]. Introducing baffles on the shell side significantly increases the overall heat transfer rate, optimizes the system efficiency, and provides support for the tube bundles [7]. Different types of baffles, such as segmented [8, 9], disk and donut [10], and overlapped helical baffle [11], have been developed to increase heat exchanger performance. Although introducing baffles on the shell side increases performance, it comes with associated challenges, such as increased pressure loss, dead zones, and fouling [7]. To overcome these drawbacks, helical baffles were introduced [12, 13]. These baffles consist of four approximate elliptical helicoids placed in a particular angle, which occupies a quarter of the shell side. This helical configuration effectively forces the flow on the shell side into a plug flow, which performs better than segmented baffles [7], and has a smooth transition of pressure loss and velocity distribution on the shell side with increased heat transfer performance [11, 14, 15]. Over the last two decades, extensive experimental and numerical researches have been conducted to identify bottlenecks and optimize the helical baffle configuration [15–19]. A detailed investigation of baffle angle, baffle position, and their respective performance is documented [20–23]. Experimental observations show a 10% increase in heat transfer rate for the same pressure loss compared to traditional segmental baffles [20].

All the considerations have been done for standalone liquid-to-liquid heat exchangers. To the best of our knowledge, continuous helical baffle configurations have not been utilized in any AHU so far. Here we report on the integration of continuous helical baffles on the shell side which enables a combination of cross flow and counter flow. Furthermore, it forms a helical flow on the shell side, which introduces turbulence due to flow separation from the tube outer surface and enhances local mixing, which in turn increases overall system performance helping to eliminate dead-zone on the shell side. The pressure loss is significantly lower compared to the disk and donut or segmental helical baffle configurations.

Usually, metals such as aluminum, nickel, or stainless steel are used in heat exchangers due to their favorable thermal properties. Susceptibility to corrosion and

erosion, however, makes operating these heat exchangers in a damp and/or highly humid environment challenging. Furthermore, higher costs associated with commissioning and maintenance prompted the industry to look for viable alternatives. Polymers are non-corrosive, hydrophobic, and with a smooth inert surface poorly suitable for microorganisms and bio-films. Optimal hygiene and antibacterial properties can also be integrated easily [24–26]. One of the major challenges with polymers, however, is their lower thermal conductivity. Over the last two decades, a lot of research effort has been invested in improving the thermal performance of polymer composite materials. A comprehensive summary of recent advancement as well as applicability and associated challenges of composite polymers in heat exchangers can be found in [27–32]. Using very thin tube walls, it is possible to compensate for the low thermal conductivity of the plastic materials. Both experimental and numerical investigations in terms of material and design are ongoing for a suitable air-to-air heat exchanger for ventilation systems [33–37].

In this paper, we study a polymer composite recuperative shell and tube heat exchanger with continuous helical baffles, which exhibits at least 80% heat recovery efficiency over a wide temperature range. The maximum allowable pressure loss has been prescribed to be 250 Pa in accordance with [38]. In the subsequent sections, we present detailed description of the considered geometry, followed by the outcome of the numerical investigation.

2 Computational domain and governing equations

In the presented study, two geometries with different shell inner diameter have been investigated. Figure 1 presents the computer-aided design (CAD) of the considered shell and tube heat exchanger with continuous helical baffles. The outside air enters the heat exchanger through the circular inlet labeled “Inlet outside” in Fig. 1a and washes over the tube bundle, before exiting through the “Outlet outside.” The baffles guide the flow over the tube bundle to follow a helical path. The air from the room enters the exchanger through the circular inlet termed “Inlet room” and passes through the tube in a straight path before exiting the domain through the exhaust termed “Outlet room.” To eliminate the influence of the backflow inside the core section, the room air inlet and fresh air outlet are placed 150 mm away from the heat exchanger core. The flow is driven by a constant volume flow rate normal to boundary at the inlets. Initially, a set of 3 counterflow heat exchangers, consisting of 310, 417, and 647 tubes, have been studied.

To minimize the pressure drop and maximize compactness on the shell side, tubes are placed in a triangular pitch layout. The heat exchanger core has an outer

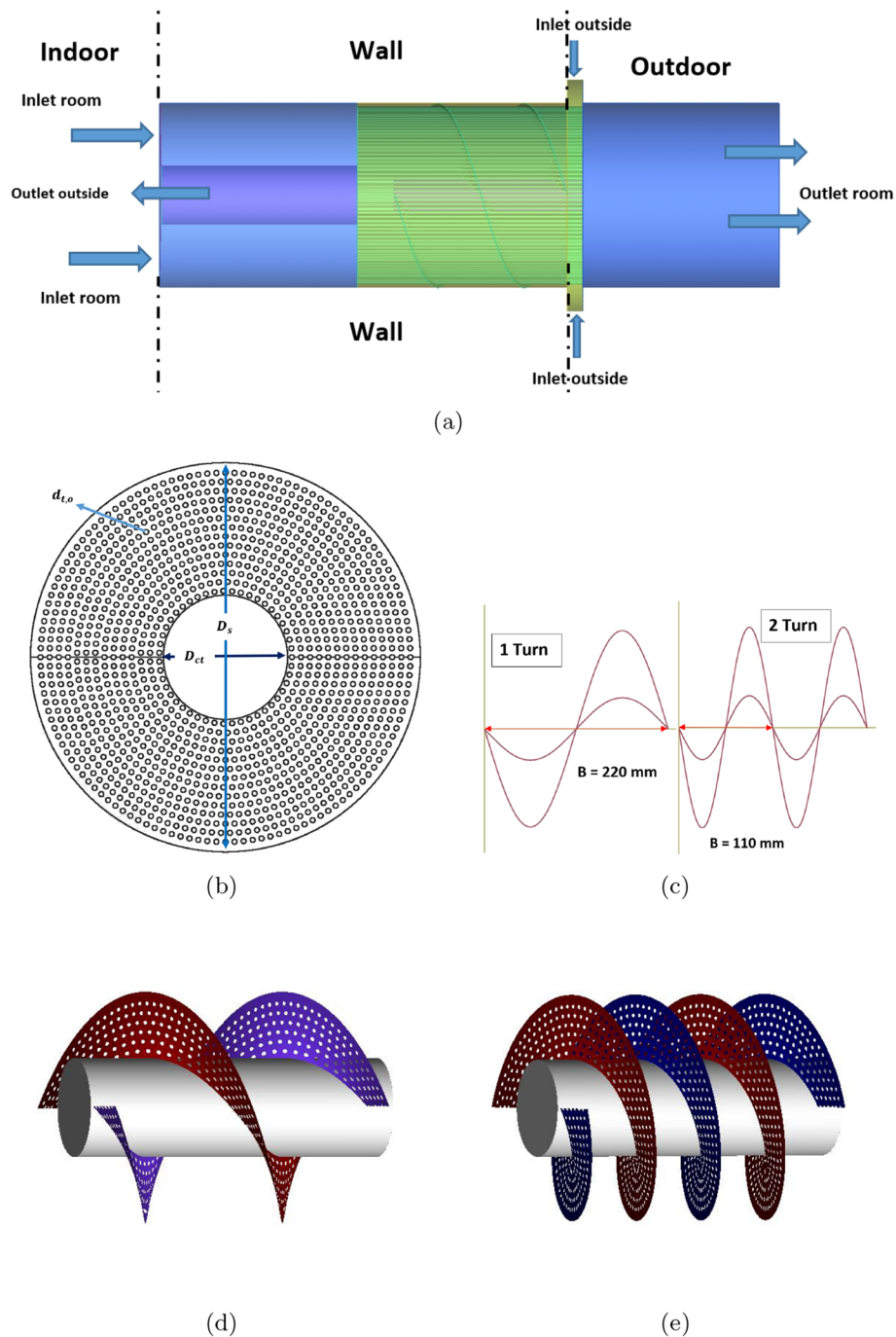


Fig. 1 Overview of **a** heat exchanger geometry. **b** Tube outer diameter $t_{d,o}$, shell inner diameter D_s , and center tube diameter D_{ct} . **c** Baffle pitch B for 1 turn and 2 turn depicting outer and inner helix. **d, e** 1/2-turn helical baffle with the center support tube

diameter of 175 mm and a tube length of 290 mm. Two co-rotating baffles with a baffle pitch of 220 mm and 110 mm, respectively, are integrated on the shell side. For simplicity, these two configurations are referred to as 1-turn and 2-turn baffles in the proceeding sections. In the next

step, another heat exchanger with identical dimensions has been considered. The only variation has been the shell inner diameter, which has been increased from 175 to 230 mm with baffle pitch of 220 mm. In Table 1, dimensions of the considered geometries are summarized.

Table 1 Geometric parameters for the two designs with 1- and 2-turn helical baffles

Item	Dimensions	Geometry 1	Geometry 2
Shell parameter	D_s [mm]	175	230
Tube parameter	$d_{t,o}$ [mm]	3.5	3.5
	Length [mm]	290	290
	Thickness [mm]	0.6	0.6
	Pitch S [mm]	6.2	6.2
Baffles	Pitch B [mm]		
	1-turn	220	220
	2-turn	110	
	Thickness [mm]	0.6	0.6
	No of baffles	2	2, 3, 4, and 12
Angles	21.89° and 11.3°	16.59°	

The working fluid is considered to be compressible, with the thermophysical properties set as temperature dependent. The thermophysical properties of the heat exchanging tube and baffles are considered constant. The unsteady Reynolds Averaged Navier-Stokes (RANS) equations are considered to describe the flow of a compressible fluid and are given as [39],

$$\frac{\partial \rho}{\partial t} + \frac{\partial}{\partial x_i}(\rho u_i) = 0 \quad (1)$$

$$\frac{\partial}{\partial t}(\rho u_i) + \frac{\partial}{\partial x_i}(\rho u_i u_i) = -\frac{\partial p}{\partial x_i} + \frac{\partial}{\partial x_j} \left[\mu \left(\frac{\partial u_i}{\partial x_j} + \frac{\partial u_j}{\partial x_i} - \frac{2}{3} \delta_{ij} \frac{\partial u_k}{\partial x_k} \right) \right] + \frac{\partial \tau_{ij}^R}{\partial x_j} \quad (2)$$

$$\frac{\partial}{\partial t}(\rho E) + \frac{\partial}{\partial x_j}(u_j(\rho E + p)) = \frac{\partial}{\partial x_j} \left(k_{eff} \frac{\partial T}{\partial x_j} + \tau_{i,j}^{eff} u_i \right) + S_h \quad (3)$$

Equations (1), (2), and (3) correspond to mass, momentum, and energy conservation equations respectively and ρ , u_i , and E represents the Reynolds averaged

$$\frac{\partial(\rho \omega)}{\partial t} + \frac{\partial(\rho \omega u_j)}{\partial x_j} = P_\omega + D_\omega + \frac{\partial}{\partial x_j} \left[(\mu + \sigma_\omega \mu_t) \frac{\partial \omega}{\partial x_j} \right] + 2(1 - F_1) \frac{\rho \sigma_\omega 2}{\omega} \frac{\partial k}{\partial x_j} \frac{\partial \omega}{\partial x_j} \quad (8)$$

density, velocity, and energy of the considered fluid. Here $\tau_{ij}^R = (-\rho \overline{u'_i u'_j})$ in (2) is the Reynolds stress tensor and should be modeled accordingly to have a closed system. Within the energy conservation equation, the effective thermal conductivity is defined as $k_{eff} = k + k_t$ and the turbulent thermal conductivity k_t is defined according to the chosen turbulence model. The viscous dissipation term, $\tau_{i,j}^{eff} u_i$, is only activated if the Brinkman number $\frac{\mu u^2}{\kappa \Delta T}$ approaches or exceeds the value 1. Here, ΔT corresponds to the system temperature difference and is enabled by default for density-based

solvers. S_h is the heat source, either due to radiation or due to joules heating. In the energy Eq. (3), E is defined as

$$E = h - \frac{p}{\rho} + \frac{u_i^2}{2} \quad (4)$$

where h is the sensible enthalpy of the system, p is the pressure, and u_i is the velocity.

The tubes act as obstacles on the shell side, which results in flow separation from the tube surface and baffles also have potential to introduce fluid-induced vibration [19, 22]. Hence, to model turbulent flow behavior, the 4-equation transition Shear Stress Transport (SST) [39, 40] model has been utilized. The transition SST model has been widely used to investigate the flow on the shell side of tube bundle heat exchangers [41–43]. The transition SST model is developed, by coupling two additional equations [39, 40] for intermittency γ and the transition onset criterion in terms of momentum thickness Reynolds number $R\tilde{e}_{\theta t}$ [44] with the SST $k-\omega$ model [45]. This model effectively combines $k-\omega$ and $k-\epsilon$ models to capture the flow behavior near the wall and far away from the wall, respectively. This model is a good choice for wall bounded flows [39], performs better with adverse pressure gradients, and is consequently better for flows with flow separation [46]. The resulting set of equations reads:

$$\frac{\partial(\rho \gamma)}{\partial t} + \frac{\partial(\rho U_j \gamma)}{\partial x_j} = P_\gamma - E_\gamma + \frac{\partial}{\partial x_j} \left[\left(\mu + \frac{\mu_t}{\sigma_\gamma} \right) \frac{\partial \gamma}{\partial x_j} \right] \quad (5)$$

$$\frac{\partial(\rho R\tilde{e}_{\theta t})}{\partial t} + \frac{\partial(\rho U_j R\tilde{e}_{\theta t})}{\partial x_j} = P_{\theta t} + \frac{\partial}{\partial x_j} \left[\sigma_{\theta t} (\mu + \mu_t) \frac{\partial R\tilde{e}_{\theta t}}{\partial x_j} \right] \quad (6)$$

$$\frac{\partial}{\partial t}(\rho k) + \frac{\partial}{\partial x_j}(\rho k u_j) = \tilde{P}_k + \tilde{D}_k + \frac{\partial}{\partial x_j} \left[(\mu + \sigma_k \mu_t) \frac{\partial k}{\partial x_j} \right] \quad (7)$$

Equation (5) is the transport equation for intermittency γ where P_γ is the transition source terms and E_γ is the destruction/relaminarization source. Equation (6) is the transport equation for the transition momentum thickness Reynolds number $R\tilde{e}_{\theta t}$. In (7), the source terms are given as $\tilde{P}_k = \gamma_{eff} P_k$ and $\tilde{D}_k = \min(\max(\gamma_{eff}, 0.1), 1.0) D_k$. Here, P_k and D_k are the production and destruction of turbulent kinetic energy κ respectively. In (8) P_ω and D_ω are the production and destruction of the turbulence dissipation rate ω respectively and F_1 is responsible switching between the $k-\omega$

and $k-\epsilon$ turbulence model. The detailed description is omitted here. Interested readers are referred to the comprehensive description given in references [39, 40, 44].

The Peng-Robinson equation of state is used to account for the density variation with respect to temperature [47]. The inlets of the incoming fresh air and outgoing room air are specified as a mass-flow-inlet. To maintain the same volume flow rate on both shell and tube side, for inlets of the incoming fresh air and outgoing room air, the mass flow rate has been specified according to the temperature and density of the fluid. The outlets are modeled as pressure outlets. The exterior wall of the heat exchanger is modeled as adiabatic to exclude the influence of the surrounding temperature on the heat exchanger. It is justified, as the heat exchanger will be equipped with a thermal insulation prior to installation. The exterior walls, as well as the tube walls, are specified to be no-slip walls. The tube walls are modeled as zero-thickness walls and fluent automatically creates a shadow zone to account for the two adjacent sides of tube and shell.

A pressure-based solver in fluent has been used for the presented simulated data. The governing equations are discretized using the finite volume method (FVM) and iteratively solved using a coupled algorithm, which solves momentum and pressure-based continuity equation together. Second order schemes have been used for spatial discretization of the momentum and pressure equations and first order accurate schemes for the turbulence model equations with the convergence criterion for all the variables has been specified to be 10^{-6} .

The equations used for post-processing are shown as follows:

1. The heat recovery efficiency is measured as [48]

$$\epsilon = \frac{T_{fresh,out} - T_{fresh,in}}{T_{room,in} - T_{room,out}} \quad (9)$$

Here, $T_{fresh,in}$ and $T_{fresh,out}$ are the temperatures at the corresponding inlet and outlet of the incoming fresh air, respectively. Similarly, $T_{room,in}$ and $T_{room,out}$ are the temperatures at the inlet and outlet of the outgoing room air. It should be noted that the efficiency refers only to the sensible heat exchange between the two fluids, without considering the energy consumption by the driving fan.

2. Δp is obtained by comparing the pressure at the inlet and outlet. Δp on the shell side is calculated using (10) where $P_{fresh,in}$ is the pressure at the fresh air inlet and $P_{fresh,out}$ is the pressure at fresh air outlet pressure at the end of the simulation.

$$\Delta p = P_{fresh,in} - P_{fresh,out} \quad (10)$$

3. Heat transfer rate \dot{Q} on the shell side is calculated as [22]

$$\dot{Q} = \dot{m}c_p(T_{fresh,out} - T_{fresh,in}) \quad (11)$$

Here, \dot{m} and c_p are the mass flow rate and the corresponding specific heat, respectively. The overall heat transfer coefficient U is

$$U = \frac{\dot{Q}}{A_t \Delta T_{LM}} \quad (12)$$

$$\text{where } \Delta T_{LM} = \frac{\Delta T_1 - \Delta T_2}{\ln(\Delta T_1 / \Delta T_2)} \quad (13)$$

$$\text{with } \Delta T_1 = T_{hot,in} - T_{cold,out} \quad (14)$$

$$\text{and } \Delta T_2 = T_{hot,out} - T_{cold,in} \quad (15)$$

Here A_t is the heat transfer surface defined as the total outer surface of the tubes and ΔT_{LM} is the log mean temperature difference.

4. Average velocity $u_{avg,s}$ on the shell side [20]

$$u_{avg,s} = \frac{\dot{V}}{A_c} \quad (16)$$

$$A_c = 0.5 \left(1 - \frac{D_{ct}}{D_{s,in}} \right) B D_{s,in} \left(1 - \frac{d_{t,o}}{S} \right) \quad (17)$$

Here, \dot{V} , A_c , D_{ct} , S , and $d_{t,o}$ are the volume flow rate, characteristic cross flow area, center tube outer diameter, tube pitch, and tube outer diameter respectively.

5. Reynolds number (Re) and Nusselt number (Nu) are defined as [20]

$$Re = \frac{u_{avg,s} d_{t,o}}{\nu} \quad (18)$$

$$Nu = \frac{U d_{t,o}}{\lambda} \quad (19)$$

where ν and λ are the characteristic kinematic viscosity and thermal conductivity of the fluid respectively.

6. Effective fluid path length L_{eff} is calculated as [49]

$$L_{eff} = \frac{L_h}{B} \sqrt{(\pi D_{s,in}^2 + B^2)} \quad (20)$$

where L_h is defined as the length that is covered by the continuous helical baffles. $D_{s,in}$ and B are the shell inner diameter and baffle pitch respectively.

3 Results and discussion

Within this section, the result of the current investigations are presented. First, we report the outcome of the grid independence study. The results of the parameter study for the smaller geometry with 647 tubes made of unfilled high-density polyethylene (HDPE) are discussed first and the results for the second geometry with 1224 tubes made of composite material LNP™ KONDUIT™ OX11315 [50] are presented and discussed afterwards. OX11315 is a compound based on polyphenylene sulfide (PPS) resin containing mineral for improved thermal conductivity. In Table 3, the thermo-physical properties of the considered materials pertaining to the simulations are listed.

3.1 Grid independence study

To obtain a grid independent solution, a Grid Convergence Index (GCI) study has been performed using the five-step method [51]. For completeness, the steps are summarized as follows:

- (i) Define representative cell size, for a structured grid as

$$h = [\Delta x_{max} \Delta y_{max} \Delta z_{max}]^{\frac{1}{3}} \quad (21)$$

and for an unstructured mesh

$$h = \left[\frac{\sum_{i=1}^N V_i}{N} \right]^{1/3} \quad (22)$$

where V_i corresponds to the volume of each cell contained inside the domain and N is the total number of the control volumes.

- (ii) Select 3 significantly different grids with a grid refinement factor of $r = \frac{h_{coarse}}{h_{fine}} \geq 1.3$ and run the simulations for the variable of interest, e.g., Φ
- (iii) Let $h_1 < h_2 < h_3$ and $r_{21} = \frac{h_2}{h_1}$, $r_{32} = \frac{h_3}{h_2}$, determine the order of convergence p as

$$p = \left[\frac{1}{\ln(r_{21})} \right] \left[\ln \left| \frac{\Phi_2 - \Phi_3}{\Phi_1 - \Phi_2} \right| + q(p) \right] \quad (23)$$

$$q(p) = \ln \left(\frac{r_{21}^p - s}{r_{32}^p - s} \right) \quad (24)$$

$$s = 1. \text{sgn} \left(\frac{\Phi_2 - \Phi_1}{\Phi_2 - \Phi_1} \right) \quad (25)$$

- (iv) Since $q(P) = 0$ for a constant grid refinement factor r , i.e. $r_{21} = r_{32} = r$, the above equation for order of convergence P simplifies to

$$p = \left[\frac{1}{\ln(r)} \right] \left[\ln \left| \frac{\Phi_3 - \Phi_2}{\Phi_2 - \Phi_1} \right| \right] \quad (26)$$

- (v) Calculate the extrapolated value from equations

$$\Phi_{ext}^{21} = \frac{r_{21}^p \Phi_1 - \Phi_2}{|r_{21}^p - 1|} \quad \text{and} \quad \Phi_{ext}^{32} = \frac{r_{32}^p \Phi_2 - \Phi_3}{|r_{32}^p - 1|} \quad (27)$$

- (vi) Obtain the relative and the extrapolated error estimates for the observed order p as

$$e_a^{21} = \left| \frac{\Phi_1 - \Phi_2}{\Phi_1} \right| \quad \text{and} \quad e_{ext}^{21} = \left| \frac{\Phi_{ext}^{21} - \Phi_1}{\Phi_{ext}^{21}} \right| \quad (28)$$

- (vii) Leading to the fine Grid Convergence Index (GCI):

$$GCI^{21} = \frac{F_s \cdot e_a^{21}}{r_{21}^p - 1} \quad \text{and} \quad GCI^{32} = \frac{F_s \cdot e_a^{32}}{r_{32}^p - 1} \quad (29)$$

where $F_s = 1.25$ for comparison over three or more grids. For further details, we refer the readers to [51, 52].

Due to the complexity of geometry, the mesh has been generated using ICEM CFD. For all the generated meshes, identical configuration settings have been applied on both geometries. For both geometries, the generated mesh has the same near wall mesh resolution and adhered to the same mesh quality criterion required by FLUENT. In this section, we only present the GCI study for the tube bundle heat exchanger with a shell inner diameter of 223 mm and 1224 tubes. The geometry with the smaller shell inner diameter of 117 mm and 647 tubes with no baffle has approximately 25 million cells. That with 1- and 2-turn continuous helical baffles has approximately 30 million cells. For the GCI study for the geometry with 1224 tubes and 1–turn continuous helical baffle, three grids have been used with 34.59, 64.24, and 106.74 million cells respectively. After reaching steady state in the simulation, velocity u , temperature T , and pressure p are probed from a point located inside the shell side of the heat exchanger. The observations are summarized in Table 2. For all the three variables, an asymptotic convergence (i.e., $\frac{GCI^{21}}{GCI^{32}} \approx 1$) is observed. Yet, the obtained order of accuracy \hat{p} is observed to be higher than 2 the formal order of accuracy [52]. Nevertheless, \hat{p} is within the acceptable range of $0 < \hat{p} < 8$ [53] and the normalized relative error calculated by (28) for T and p is also less than 2% for both the intermediate and coarse mesh. Based on [54], the convergence ratio $R = \frac{\phi_3 - \phi_2}{\phi_2 - \phi_1}$ indicates monotonic convergence ($0 < R < 1$) for T and p , whereas u exhibits oscillatory convergence. The run time for the intermediate and finest mesh is approximately two and three times higher compared to the coarsest mesh. Based on

Table 2 Outcome of GCI for T , p , and u

	T	p	u
ϕ_1	285.012	12.0811	0.723068
ϕ_2	285.387	12.1997	0.75902
ϕ_3	286.427	12.3609	0.693479
\hat{p}	5.8271	1.68	3.2936
ϕ_{ext}^{21}	284.8131	11.7509	0.6794
e_a^{21}	0.13%	0.98%	4.97%
e_a^{32}	0.38%	1.32%	8.63%
e_{ext}^{21}	0.069%	2.81%	6.43%
GCI^{21}	0.1%	4.1%	5.41%
GCI^{32}	0.3%	5.1%	12.26%
$\frac{GCI^{32}}{r^p GCI^{21}}$	0.9987	0.9903	0.9527
R	0.3456	0.7357	-0.5485

the accuracy and calculation run time, the mesh with about 34.59 million cells has been chosen. Based on the presented results, this mesh is considered to be suitable for delivering mesh independent results which are presented in the following sections. Figure 2 summarizes the outcome of GCI along with the extrapolated value using Richardson extrapolation.

3.2 Geometry A : $D_s = 175$ mm

The thermophysical properties of HDPE along with the boundary conditions for the simulation are compiled

in the second row of Tables 3 and 4. In this section, the room-side air temperature is fixed at 293.15 K.

Figure 3 shows the heat recovery efficiency and the pressure loss for different numbers of tubes and baffle turns for an outside temperature of 270.15 K and a volume flow rate of 25 m³/h. As is apparent from Fig. 3a, increasing the number of tubes translates into increased heat transfer due to a large effective heat transfer area. In our study without any baffle, the heat recovery efficiency increases from around 66% to more than 80%, by about doubling the number of tubes. Figure 3b shows, however, that a higher number of tubes results in a higher pressure loss penalty on the shell side. This is due to a smaller effective cross-section area for fluid flow on the shell side. Without baffles, the pressure loss Δp is not that prominent. Introducing a baffle with a single turn results in a considerable increase in heat recovery efficiency. Yet, as can be seen in Fig. 3a, an additional turn of the baffle hardly affects the heat recovery efficiency. Only for the case of 410 tubes, a minor improvement can be accomplished. The pressure loss on the other hand dramatically increases with the second turn of the baffle. While it grows from about 6 Pa without a baffle to around 27 Pa with a single turn baffle, it increases by more than a factor of 6 to around 162 Pa by introducing a second turn of the baffle for the case of 647 tubes; see Fig. 3b. In the following, we focus on the tube bundle heat exchanger with 647 tubes

The CAD model has been constructed in such a way, that there is no gap between the baffle and the tubes, as

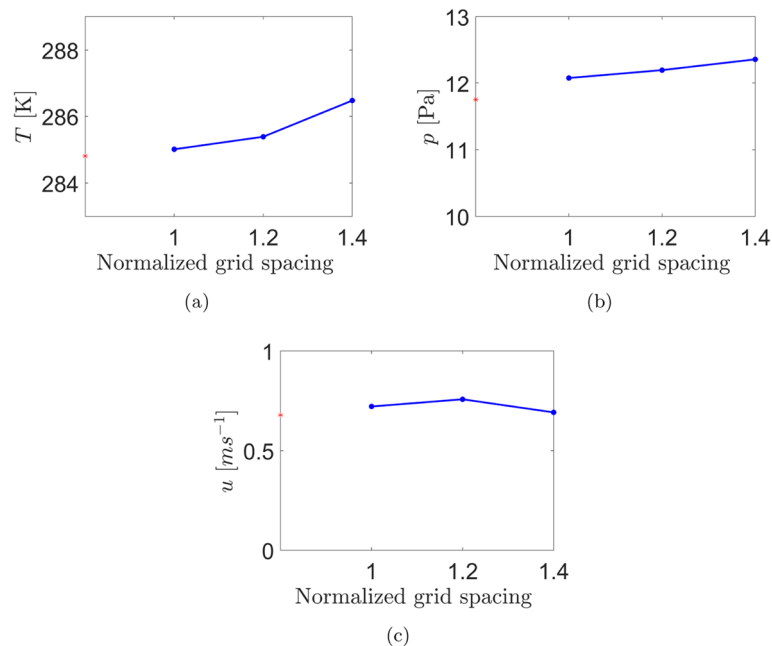


Fig. 2 Convergence of **a** temperature, **b** pressure, and **c** velocity for refined mesh. The grid spacing is normalized by the spacing of the finest mesh h_1 . Data is represented using spline to guide the eye

Table 3 Thermo-physical properties of tube materials

Tube material	HDPE	OX11315
Density [kg m ⁻³]	940	1760
Thermal conductivity [W mK ⁻¹]	0.48	3.5
Specific heat capacity [J kg ⁻¹ K ⁻¹]	1900	1260

Table 4 Boundary conditions

Tube material	Geometry A	Geometry B
Wall thickness [mm]	0.6	0.6
Tube length [mm]	290	290
Shell inner diameter [mm]	175	230
Baffle inclination angle	90°, 21.89°, 11.3°	16.59°
Inlet	Mass flow inlet	Mass flow inlet
Outlet	Pressure outlet	Pressure outlet
Outer wall	Adiabatic	Adiabatic
Room temperature [K]	293.15	293.15
Outside temperature [K]	263.15; 273.15; 283.15	243.15; 253.15; 263.15; 333.15

well as the baffle and the outer shell, to prevent leakage and bypass stream on the shell side which potentially decrease the effective mass flow rate across the tube bundles [23]. This also contributes to the increased efficiency, which is also consistent with the findings in [14] where it is reported that under identical conditions, a continuous helical baffle increases overall performance compared to non-continuous helical baffles. The continuous helical baffle forces the fluid to follow a helical path on the shell side and the flow passes over the tube bundle in an inclined cross flow manner. Hence, with a continuous helical baffle, the heat exchanger operates with cross-counter flow principle. The velocity fields for the three cases are shown in Fig. 4. It is evident that the fluid flows

along a helical path inside the shell. Furthermore, continuous helical baffles also increase the effective fluid path and decrease the cross flow area with decreasing baffle pitch. The corresponding values are listed in Table 5. This reduction of cross flow area contributes to a velocity increase inside the shell at a constant volume flow rate. Decreasing the helix angle decreases the cross flow area and increases the effective fluid path, which results in increased velocity on the shell side and consequently increases the convective heat transfer.

Figure 5a shows the heat recovery efficiency as a function of volume flow rate. The comparison demonstrates the advantage of continuous helical baffles on the heat recovery is more prominent for higher \dot{V} . For all three considered temperature differences, a change in volume flow rate has about the same impact on the heat recovery efficiency as depicted in Fig. 5b.

Pressure loss is one of the most important parameters, when evaluating the applicability of a heat exchanger, as it is directly associated with the operating cost in terms of fan power. From the Δp comparison presented in Fig. 6a, it is evident that the pressure loss increases when using helical baffles. Increasing the baffle turn from single to double, Δp increases by almost a factor of 7 for all considered \dot{V} . Figure 6b shows on the other hand that U increases with \dot{V} . This leads to the enhanced performance in terms of heat recovery. Enhanced efficiency on the shell side is attributed to the introduction of helical baffles, which increase the effective fluid path, as well as the fluid velocity due to the reduction of the effective cross flow area.

Figure 6c shows a comparison between the 3 considered cases for heat transfer coefficient per unit pressure drop. Also in terms of $U/\Delta p$ a baffle with 1 baffle with 1-turn performs better than their corresponding 2-turn counterparts for all the considered \dot{V} . The system without baffles has the lowest Δp , but also performs worst

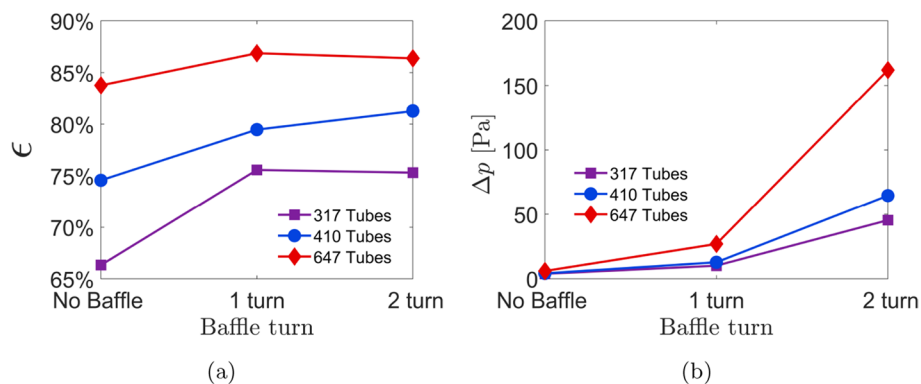


Fig. 3 Comparison of **a** heat recovery efficiency ϵ and **b** pressure loss Δp for 317, 410, and 647 tubes with and without continuous helical baffles. $T_{out} = 270.15$ K, $T_{room} = 293.15$ K, and $\dot{V} = 25$ m³/h

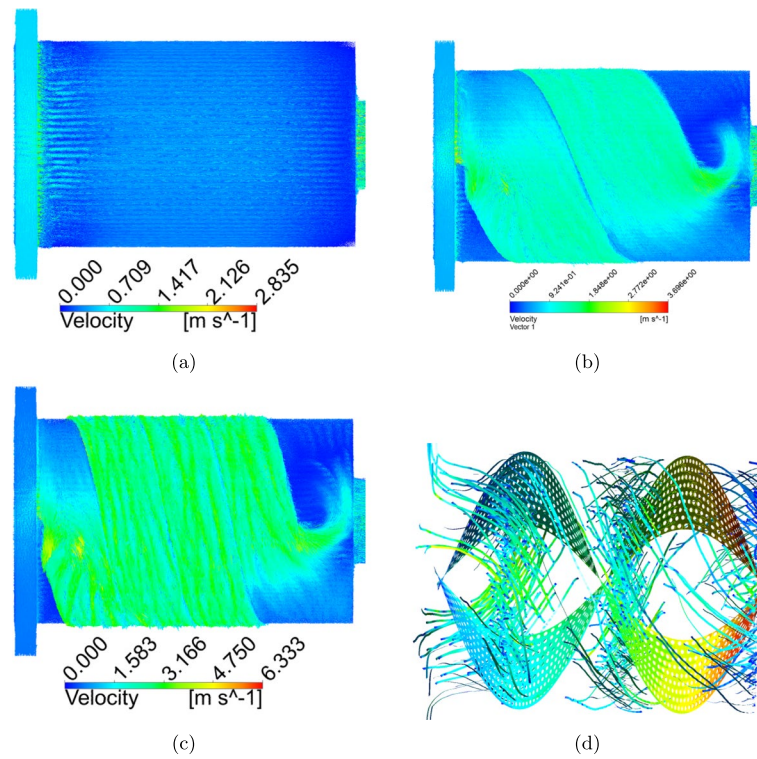


Fig. 4 Velocity field on the shell side: **a** no baffle, **b** 1-turn baffle, **c** 2-turn baffle, and **d** streamlines at $\Delta T = 10\text{ K}$ and $\dot{V} = 30\text{ m}^3/\text{h}$

Table 5 Effective fluid path and cross flow area

Baffle turn	L_{eff} [mm]	A_c [m ²]
0	290	0.0107
1	662.16	0.0035
2	1191.35	0.0018

in terms of heat recovery efficiency. On the other hand, the system with 2-turn baffles has the lowest heat transfer coefficient per unit pressure drop. However, efficiency gain is not that significant as shown in Fig. 5a.

From the discussion above, it can be summarized that the continuous helical baffles forces the fluid to follow a helical path, which helps to reduce dead zones, and as the fluid passes the tube bundle in an inclined way, it helps to

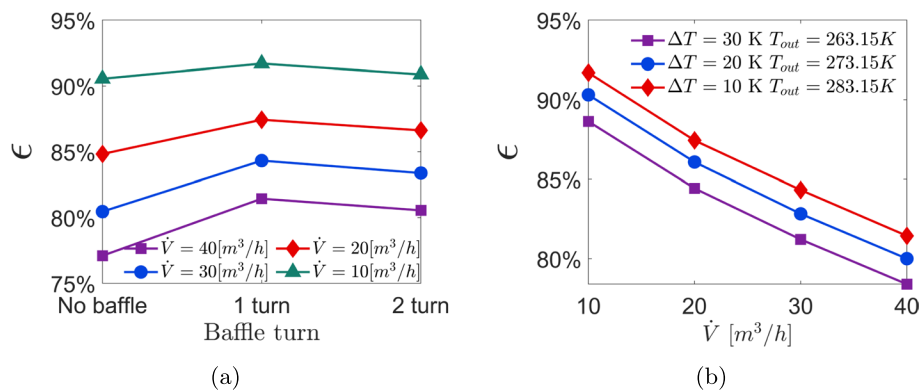


Fig. 5 Comparison of heat recovery efficiency ϵ **a** with and without continuous helical baffles for different \dot{V} and $\Delta T = 10\text{ K}$ and **b** as a function of \dot{V} for the case of a single turn baffle. Both fresh and room air inlets have identical \dot{V}

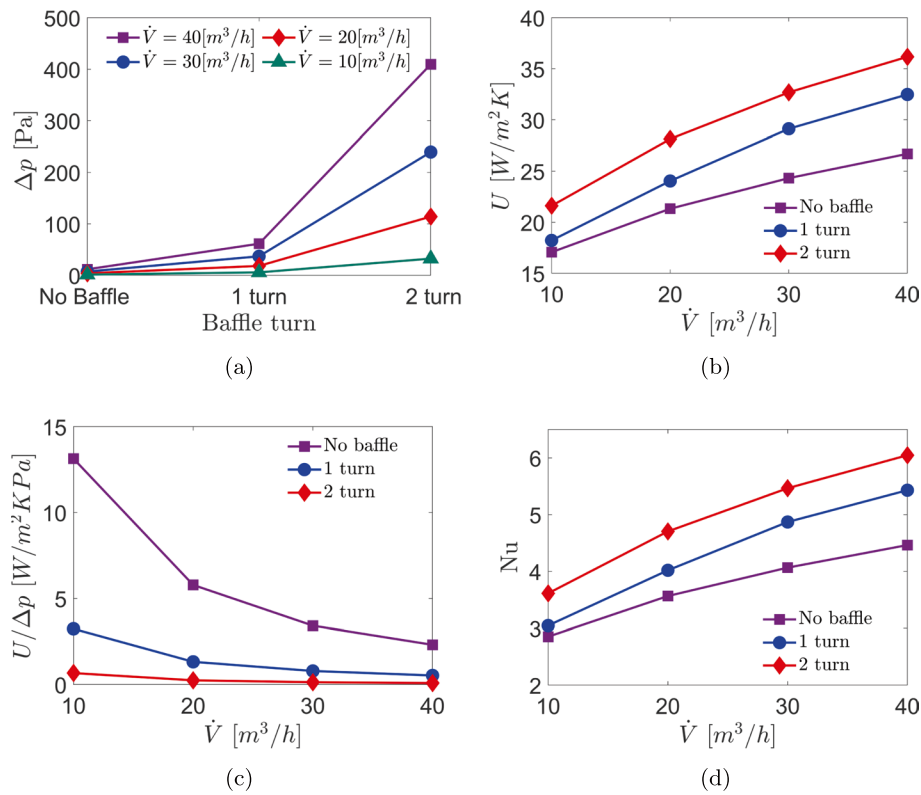


Fig. 6 Impact of the baffle turns and flow rate on **a** Δp , **b** U , **c** $U/\Delta p$, and **d** Nu at $\Delta T = 10K$

reduce flow induced vibrations [22]. It also increases the effective fluid path and contracts the effective cross flow area, which in turn increases the convective heat transfer [14]. However, enhanced performance in terms of heat recovery efficiency comes at a cost of higher pressure loss. For the considered geometry with continuous baffles of more than a single turn, pressure loss drastically increased, while the efficiency gain is not significant.

3.3 Geometry B : $D_s = 230$ mm

As shown, increasing the tube count and introducing continuous helical baffles improve heat recovery efficiency significantly at the expense of a minor pressure loss penalty. Increasing the baffle turn from 1 to 2 by reducing the baffle pitch, however, has shown no significant improvement. Instead, it increases the pressure loss dramatically on the shell side. Yet, increasing the total number of co-rotating baffles may help homogenizing temperature and velocity distributions inside the shell and at the outlet. With these considerations, we now study the impact of the number of baffles, each having a single turn. From here onward, we present the data for a geometry with shell inner diameter $D_s = 230$ mm, with 1224 tubes of 290 mm length and with 3, 4,

and 12 single turn continuous helical baffles. Figure 7 shows the considered configuration with 12 baffles.

In comparison to HDPE, the composite material OX11315 performs better in terms of heat recovery efficiency for identical boundary conditions on the modified geometry. The observed heat recovery efficiency is around 79% for HDPE and 81% for OX11315. Indoor and outdoor temperature has been fixed at 293.15 K and 263.15 K respectively with $\dot{V} = 40 m^3/h$.

Variation trends of temperature distribution at the outlet of incoming fresh air on the room side are shown in Fig. 8. From the contour plots at the outlet, it is evident that increasing number of individual helical baffles on the shell side helps to obtain a more homogeneous temperature distribution.

As shown in Fig. 9, introducing continuous helical baffles increases the pressure drop on the shell side. Yet, increasing the number of co-rotating baffles from 2 to 12 results in enhanced Δp from about 10 Pa to about, 49 Pa which is still well below the prescribed value of 250 Pa for the considered case. However, there is no considerable improvement in terms of heat recovery efficiency, which is about 78% for the data presented in Fig. 9.

The flow field development on the shell side is shown for the case of 12 baffles in Fig. 10a. The air enters the

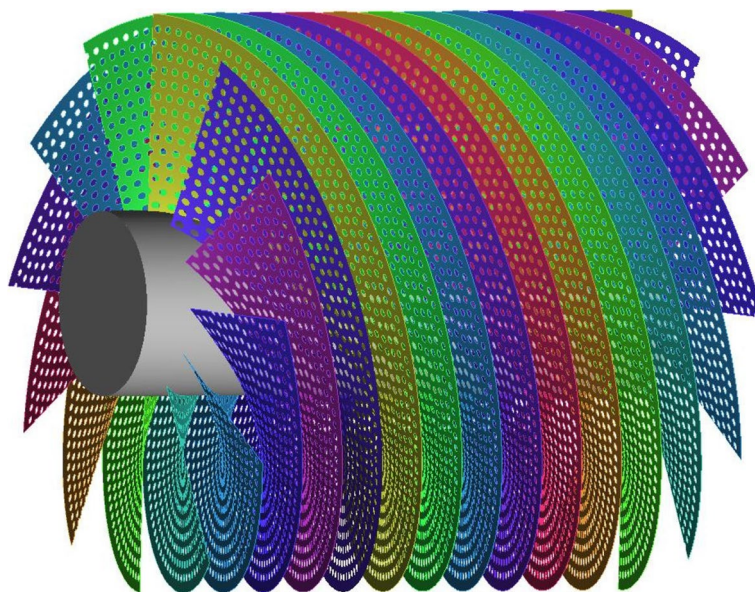


Fig. 7 12 continuous co-rotating helical baffle (Geometry B)

domain through the inlet and passes through the grooves between the baffles in a helical manner. The streamline colors indicate the absolute velocity. In Fig. 10b, the velocity contours at the outlet shows a homogeneous velocity distribution. As the fluid follows a helical path inside the shell, there exist neither any stagnation zone nor the flow experience any localized re-circulation and/or stagnation near the shell inner wall. Therefore, the velocity distribution is smooth inside the shell, and as there is no abrupt change in the flow direction, dead zone simple does not occur. Consequently, this helps to reduce pressure drop on the shell side and the flow is guided smoothly by the baffles. This is consistent with previous works, where it is shown that the flow inside the shell is smooth compared to conventional segmental baffles [13, 20]. As the helix ends before the flow reaches the outlet, the flow passes through a straight section and the velocity magnitude increases due to contraction.

Figure 11 visualizes the flow-rate dependent impact of different outdoor temperatures on the heat recovery efficiency and pressure drop. The heat recovery efficiency declines with the volume flow rate, similar to the other geometry with 647 tubes, as can be seen in Fig. 5b. The considered system performs with a heat recovery efficiency of more than 75% for outside temperatures as low as of 243.15 K. Figure 11 exhibits another interesting phenomenon in terms of heat recovery efficiency for cold and hot outside air temperatures: If the incoming air is hotter than room, the measured efficiency is higher than the opposite case. For the same temperature difference of 40 K, the efficiency is about 90% if the incoming air

is hotter, while the heat recovery efficiency is about 85% for low outer temperature. For further analysis, we performed two additional simulations at a flow rate $\dot{V} = 40 \text{ m}^3/\text{h}$, reversing the temperature differences: While the outer temperature was fixed at 293.15 K, the room temperature is considered to be at 253.15 K in the first case and 333.15 K in the second case. In the first case, the air cools down to 255.3 K, i.e., the heat recovery efficiency increases to 94.7%, while the efficiency is about 89% in the second case. In the first case, we observe an efficiency increase from about 79% to 94.7% and for the second case slight decrease from 91% to 89%. This again complements the continuous helical baffle design for heat recovery efficiency. The heat capacity rate of the coldest air at 253.15 K is $0.0156 \text{ Jkg}^{-1}\text{K}^{-1}$, air at 293.15 K is $0.0135 \text{ Jkg}^{-1}\text{K}^{-1}$ and the warmest air at 333.15 K is $0.0119 \text{ Jkg}^{-1}\text{K}^{-1}$. The reason for the difference in efficiency is that the fluid with the smallest heat capacity rate experiences the larger temperature change, i.e., the rate of heat transfer needed to change the temperature of the fluid stream by 1K as it flows through a heat exchanger. The air at 333.15 K experiences the largest temperature change and therefore the heat recovery efficiency is higher in comparison to the air at 253.15 K for the same $\Delta T = 40 \text{ K}$.

The heat transfer rate \dot{Q} and overall heat transfer coefficient U are the important parameters for the evaluation of a heat exchanger. In Fig. 12, the impact of \dot{V} on both parameters are presented. Heat transfer rate increases with volume flow rate, as shown in Fig. 12a. This can be traced back to the fact that the thermal boundary layer decreases with increased volume flow rate and increases

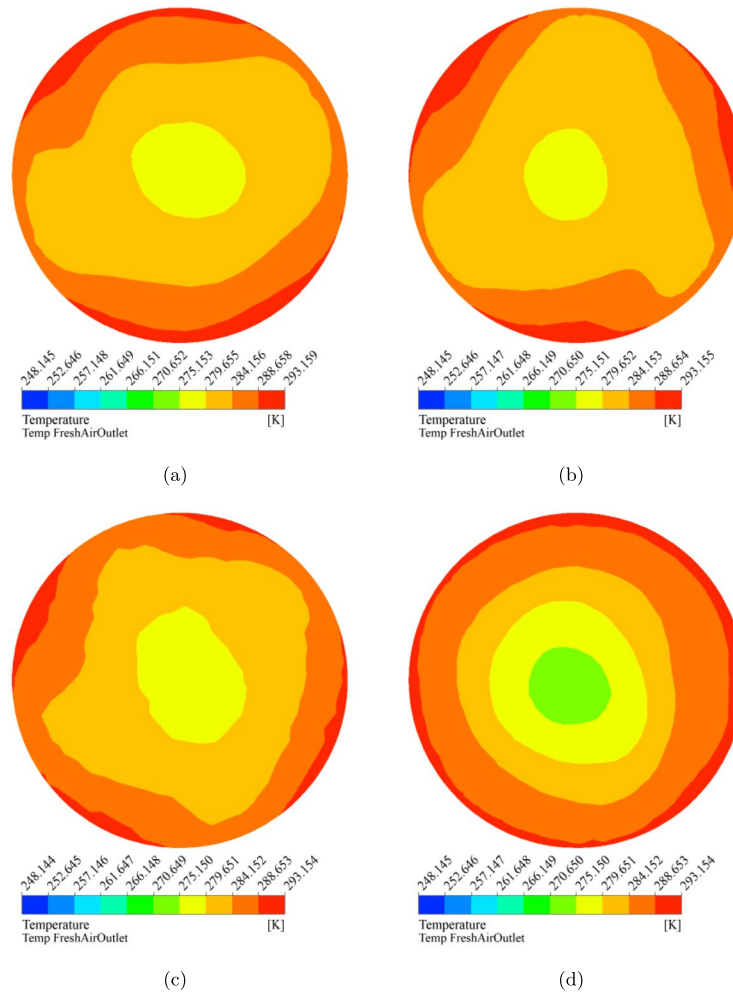


Fig. 8 Temperature distribution of fresh air at the outlet for **a** 2, **b** 3, **c** 4, and **d** 12 baffles

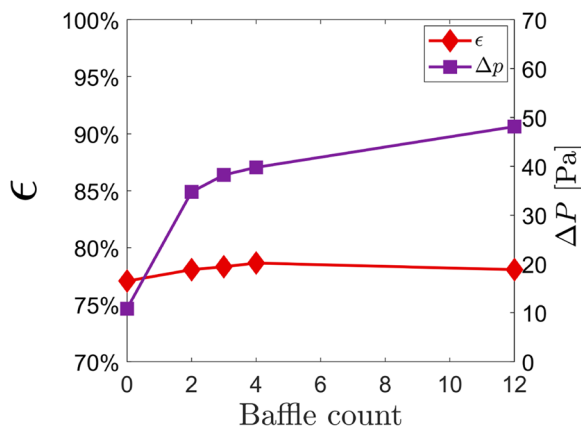


Fig. 9 Efficiency ϵ and pressure loss ΔP vs number of baffles. Introduction of additional co-rotating baffles on the shell side does not have any detrimental impact in terms of ΔP . Comparison is done for $\dot{V} = 40 \text{ m}^3/\text{h}$ and $\Delta T = 50 \text{ K}$

the overall heat transfer. As such, higher flow rates result in a higher overall heat transfer coefficient, as shown in Figs. 6b and 12b.

In this section, we investigate the thermal-hydraulic performance of a tube bundle heat exchanger with 12 continuous helical baffles. The original geometry is modified by increasing the inner diameter of the shell to accommodate additional tubes, which positively impacts performance by increasing the effective heat exchange area. The outcome of the study clearly showcases the benefit of introducing continuous helical baffles, as it increases the heat recovery efficiency to above 80% for a large temperature spectrum relevant to ventilation system while keeping the pressure loss within the prescribed maximum of 250 Pa. Furthermore, increasing the baffle count from 2 to 12 helps to homogenize the temperature and velocity distribution at the outlet without having a negative impact on the shell side pressure loss.

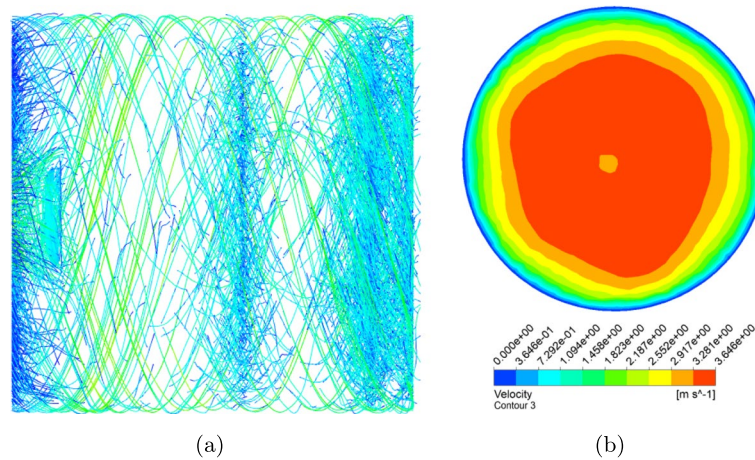


Fig. 10 **a** Velocity streamline of a 12 baffle model and **b** velocity contour at the outlet for outside air for $\Delta T = 40\text{ K}$ and $\dot{V} = 30\text{ m}^3/\text{h}$

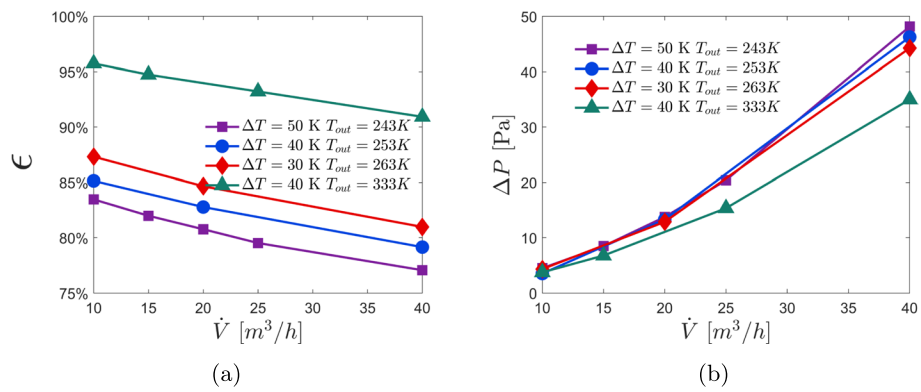


Fig. 11 **a** Efficiency ϵ and **b** pressure drop Δp as a function of volume flow rate. Room temperature is kept fixed at 20°C (293.15 K)

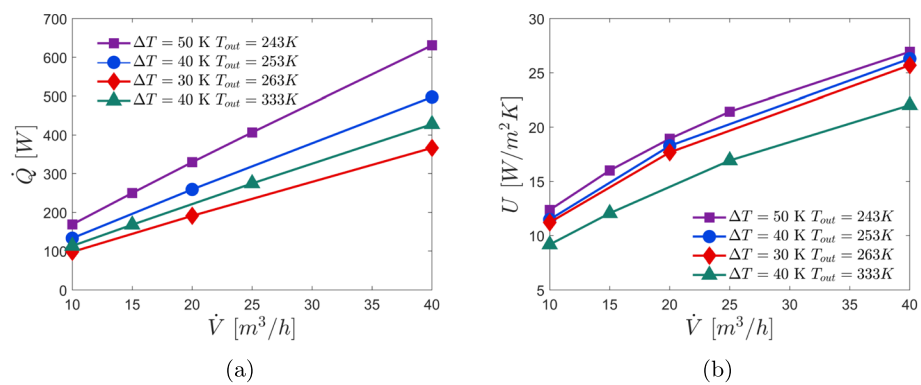


Fig. 12 **a** Heat transfer rate \dot{Q} and **b** overall heat transfer coefficient U as a function of \dot{V}

4 Conclusion

The numerical study examines the suitability of a compact tube bundle heat exchanger made of composite material to be integrated into an air handling unit.

Continuous helical baffles increase the effective flow path and force the flow to follow a helical path. Due to an increase in velocity, resulting from a decreasing cross flow area, the convective heat transfer rate rises.

The baffles serve as support for the tube bundle with a smooth flow path and thus help to eliminate potential dead zones. The system performs best with a single turn and introducing a second turn does not have a positive impact on the heat recovery efficiency. Introducing multiple co-rotating helical baffles yields a more homogeneous temperature distribution at the outlet and at the same time serves as increased support for the tube bundle. The study shows that the system can deliver heat recovery efficiency beyond 80% for a wide range of outdoor temperatures, i.e., between 243.15 K and 333.15 K. Low pressure loss at maximum volume flow rate of 40m³/h with increased heat recovery efficiency makes it a viable candidate for an energy efficient heat exchanger solution for integration into ventilation systems.

5 Nomenclature

<i>AHU</i>	Air handling units
<i>EU</i>	European Union
<i>CAD</i>	Computer-aided design
<i>RANS</i>	Reynolds Averaged Navier-Stokes
<i>GCI</i>	Grid Convergence Index
<i>B</i>	Baffle pitch
<i>D_s</i>	Shell inner diameter
<i>D_{c,t}</i>	Center tube diameter
<i>t_{d,o}</i>	Tube outer diameter
ϵ	Heat recovery efficiency
\dot{Q}	Heat transfer rate
<i>U</i>	Overall heat transfer coefficient
<i>m</i>	Mass flow rate
<i>c_p</i>	Specific heat
<i>V</i>	Volume flow rate
<i>A_c</i>	Characteristic cross flow area
<i>L_{eff}</i>	Effective fluid path length
<i>P</i>	Order of convergence
Φ	Variable of interest
<i>T</i>	Temperature
<i>p</i>	Pressure
<i>E</i>	Energy
<i>u_i</i>	Velocity
<i>Re</i>	Reynolds number
<i>Nu</i>	Nusselt number

Acknowledgements

The authors gratefully acknowledge the financial support from the Zentrales Innovationsprogramm Mittelstand - ZIM project no: ZF4134318RH9.

We acknowledge financial support by Deutsche Forschungsgemeinschaft and Friedrich-Alexander-Universität Erlangen-Nürnberg within the funding program "Open Access Publication Funding."

Special thanks to Prof. Andreas Wierschem and Dr.-Ing. Manuel Münsch for their continuous support in writing assistance, technical editing, and editing.

Authors' contributions

The authors read and approved the final manuscript.

Funding

Open Access funding enabled and organized by Projekt DEAL. This project is supported by Zentrales Innovationsprogramm Mittelstand - ZIM, project no: ZF4134318RH9.

Availability of data and materials

The datasets generated during and/or analyzed during the current study are available from the corresponding author on reasonable request.

Declarations

Ethics approval and consent to participate

Not applicable.

Consent for publication

Not applicable.

Competing interests

The authors declare that they have no competing interests.

Received: 22 June 2023 Accepted: 12 December 2023

Published online: 10 January 2024

References

- Council of European Union (2018). Directive of the european parliament and of the council on the energy performance of buildings (recast) (COM/2021/802 final). <https://eur-lex.europa.eu/legal-content/EN/TXT/?uri=celex:52021PC0802>. Accessed 27 Dec 2023
- Federal Ministry for Economic Affairs and Energy (BMWi) (2010). Energy efficiency made in germany. https://www.bmwk.de/Redaktion/EN/Publikationen/2010-energy-efficiency-made-in-germany.pdf?_blob=publicationFile&v=1. Accessed 27 Dec 2023
- European Commission and Joint Research Centre and Martirano, G and Pignatelli, F and Vinci, F and Hernández Moral, G and Serna-González, V and Ramos-Díez, I and Valmaseda, C and Coors, V and Fitzky, M and Struck, C (2022). *Comparative analysis of different methodologies and datasets for energy performance labelling of buildings*. <https://doi.org/10.2760/746342>
- Federal Ministry for Economic Affairs and Climate Action (BMWK) (2022). Renewable energy sources in figures national and international developments, 2021. <https://www.erneuerbare-energien.de/EE/Redaktion/DE/Downloads/Berichte/renewable-energy-sources-in-figures-2021.html>
- Bell, K. J. (2005). Heat exchanger design for the process industries. *Journal of Heat Transfer*, 126(6), 877–885. <https://doi.org/10.1115/1.1833366>
- Master, B. I., Chunangad, K. S., Boxma, A. J., Kral, D., & Stehlik, P. (2006). Most frequently used heat exchangers from pioneering research to worldwide applications. *Heat Transfer Engineering*, 27(6), 4–11. <https://doi.org/10.1080/01457630600671960>
- Stehlik, P., & Wadekar, V. V. (2002). Different strategies to improve industrial heat exchange. *Heat Transfer Engineering*, 23(6), 36–48. <https://doi.org/10.1080/01457630290098673>
- Reppich, M. & Zagermann, S. (1995). A new design method for segmentally baffled heat exchangers. *Computers & Chemical Engineering*, 19:137–142. European Symposium on Computer Aided Process Engineering 3-5. [https://doi.org/10.1016/0098-1354\(95\)87028-8](https://doi.org/10.1016/0098-1354(95)87028-8).
- EI-Said, E. M. S., & Abou Al-Sood, M. M. (2019). Shell and tube heat exchanger with new segmental baffles configurations: A comparative experimental investigation. *Applied Thermal Engineering*, 150, 803–810. <https://doi.org/10.1016/j.applthermaleng.2019.01.039>
- Li, H., & Kottke, V. (1999). Analysis of local shellside heat and mass transfer in the shell-and-tube heat exchanger with disc-and-doughnut baffles.

- International Journal of Heat and Mass Transfer*, 42(18), 3509–3521. [https://doi.org/10.1016/S0017-9310\(98\)00368-8](https://doi.org/10.1016/S0017-9310(98)00368-8)
11. Zhang, J., Li, B., Huang, W.-T., Lei, Y. G., He, Y.-L., & Tao, W. (2009). Experimental performance comparison of shell-side heat transfer for shell-and-tube heat exchangers with middle-overlapped helical baffles and segmental baffles. *Chemical Engineering Science*, 64, 1643–1653. <https://doi.org/10.1016/j.ces.2008.12.018>
 12. Sthelík, P., Némčanský, J., Kral, D., & Swanson, L. W. (1994). Comparison of correction factors for shell-and-tube heat exchangers with segmental or helical baffles. *Heat Transfer Engineering*, 15(1), 55–65. <https://doi.org/10.1080/01457639408939818>
 13. Kral, D., Sthelík, P., ploeg, H. J. V. D., & Master, B. I. (1996). Helical baffles in shell-and-tube heat exchangers, part i: Experimental verification. *Heat Transfer Engineering*, 17(1), 93–101. <https://doi.org/10.1080/01457639608939868>
 14. Yang, J.-F., Zeng, M., & Wang, Q.-W. (2014). Effects of sealing strips on shell-side flow and heat transfer performance of a heat exchanger with helical baffles. *Applied Thermal Engineering*, 64(1), 117–128. <https://doi.org/10.1016/j.applthermaleng.2013.11.064>
 15. Salahuddin, U., Bilal, M., & Ejaz, H. (2015). A review of the advancements made in helical baffles used in shell and tube heat exchangers. *International Communications in Heat and Mass Transfer*, 67, 104–108. <https://doi.org/10.1016/j.icheatmasstransfer.2015.07.005>
 16. Wang, Q., Chen, G., Chen, Q., & Zeng, M. (2010). Review of improvements on shell-and-tube heat exchangers with helical baffles. *Heat Transfer Engineering*, 31(10), 836–853. <https://doi.org/10.1080/01457630903547602>
 17. Zhang, J.-F., Guo, S.-L., Li, Z.-Z., Wang, J.-P., He, Y.-L., & Tao, W.-Q. (2013). Experimental performance comparison of shell-and-tube oil coolers with overlapped helical baffles and segmental baffles. *Applied Thermal Engineering*, 58(1), 336–343. <https://doi.org/10.1016/j.applthermaleng.2013.04.009>
 18. Cao, X., Zhang, R., Chen, D., Chen, L., Du, T., & Yu, H. (2021). Performance investigation and multi-objective optimization of helical baffle heat exchangers based on thermodynamic and economic analyses. *International Journal of Heat and Mass Transfer*, 176, 121489. <https://doi.org/10.1016/j.jheatmasstransfer.2021.121489>
 19. Naqvi, S. & Wang, Q. (2019). Numerical comparison of thermohydraulic performance and fluid-induced vibrations for sthxs with segmental, helical, and novel clamping antivibration baffles. *Energies*, 12(3). <https://doi.org/10.3390/en12030540>
 20. Peng, B., Wang, Q. W., Zhang, C., Xie, G. N., Luo, L. Q., Chen, Q. Y., & Zeng, M. (2007). An experimental study of shell-and-tube heat exchangers with continuous helical baffles. *Journal of Heat Transfer*, 129(10), 1425–1431. <https://doi.org/10.1115/1.2754878>
 21. Wang, Q.-W., Chen, G.-D., Xu, J., & Ji, Y.-P. (2010). Second-law thermodynamic comparison and maximal velocity ratio design of shell-and-tube heat exchangers with continuous helical baffles. *Journal of Heat Transfer*, 132(10), 101801. <https://doi.org/10.1115/1.4001755>
 22. Wang, Q., Chen, Q., Chen, G., & Zeng, M. (2009). Numerical investigation on combined multiple shell-pass shell-and-tube heat exchanger with continuous helical baffles. *International Journal of Heat and Mass Transfer*, 52, 1214–1222.
 23. Lei, Y.-G., He, Y.-L., Li, R., & Gao, Y.-F. (2008). Effects of baffle inclination angle on flow and heat transfer of a heat exchanger with helical baffles. *Chemical Engineering and Processing: Process Intensification*, 47(12), 2336–2345. <https://doi.org/10.1016/j.ccep.2008.01.012>
 24. Kasi, G., Gnanasekar, S., Zhang, K., Kang, E. T., & Xu, L. Q. (2022). Polyurethane-based composites with promising antibacterial properties. *Journal of Applied Polymer Science*, 139(20), 52181. <https://doi.org/10.1002/app.52181>
 25. Villani, M., Consonni, R., Canetti, M., Bertoglio, F., Iervese, S., Bruni, G., Visai, L., Iannace, S., Bertini, F. (2020). Polyurethane-based composites: Effects of antibacterial fillers on the physical-mechanical behavior of thermoplastic polyurethanes. *Polymers*, 12(2). <https://doi.org/10.3390/polym12020362>
 26. Zhang, Y., Huang, L., Dong, T., Li, B., & Zhang, Y. (2022). Preparation, characterization and antibacterial properties of thermoplastic chitosan/nano zno composites. *Materials Technology*, 37(11), 1846–1853. <https://doi.org/10.1080/10667857.2021.1990459>
 27. Cevallos, J. G., Bergles, A. E., Bar-Cohen, A., Rodgers, P., & Gupta, S. K. (2012). Polymer heat exchangers—history, opportunities, and challenges. *Heat Transfer Engineering*, 33(13), 1075–1093. <https://doi.org/10.1080/01457632.2012.663654>
 28. Glade, H., Moses, D., Orth, T. D. (2018). *Polymer Composite Heat Exchangers*, pages 53–116. https://doi.org/10.1007/978-3-319-71641-1_2
 29. Chen, H., Ginzburg, V. V., Yang, J., Yang, Y., Liu, W., Huang, Y., Du, L., Chen, B. (2016a). Thermal conductivity of polymer-based composites: Fundamentals and applications. *Progress in Polymer Science*, 59:41–85. Topical Volume Hybrids. <https://doi.org/10.1016/j.progpolymsci.2016.03.001>
 30. Hussain, A. R. J., Alahyari, A. A., Eastman, S. A., Thibaud-Erkey, C., Johnston, S., & Sobkowicz, M. J. (2017). Review of polymers for heat exchanger applications: Factors concerning thermal conductivity. *Applied Thermal Engineering*, 113, 1118–1127. <https://doi.org/10.1016/j.applthermaleng.2016.11.041>
 31. Chen, X., Su, Y., Reay, D., & Riffat, S. (2016). Recent research developments in polymer heat exchangers - a review. *Renewable and Sustainable Energy Reviews*, 60, 1367–1386. <https://doi.org/10.1016/j.rser.2016.03.024>
 32. Krásný, I., Astrouki, I., & Raudenský, M. (2016). Polymeric hollow fiber heat exchanger as an automotive radiator. *Applied Thermal Engineering*, 108, 798–803. <https://doi.org/10.1016/j.applthermaleng.2016.07.181>
 33. Smith, K. M., & Svendsen, S. (2015). Development of a plastic rotary heat exchanger for room-based ventilation in existing apartments. *Energy and Buildings*, 107, 1–10. <https://doi.org/10.1016/j.enbuild.2015.07.061>
 34. Kragh, J., Rose, J., Nielsen, T., & Svendsen, S. (2007). New counter flow heat exchanger designed for ventilation systems in cold climates. *Energy and Buildings*, 39(11), 1151–1158. <https://doi.org/10.1016/j.enbuild.2006.12.008>
 35. Diao, Y., Liang, L., Kang, Y., Zhao, Y., Wang, Z., & Zhu, T. (2017). Experimental study on the heat recovery characteristic of a heat exchanger based on a flat micro-heat pipe array for the ventilation of residential buildings. *Energy and Buildings*, 152, 448–457. <https://doi.org/10.1016/j.enbuild.2017.07.045>
 36. Smith, K. M., & Svendsen, S. (2016). The effect of a rotary heat exchanger in room-based ventilation on indoor humidity in existing apartments in temperate climates. *Energy and Buildings*, 116, 349–361. <https://doi.org/10.1016/j.enbuild.2015.12.025>
 37. Górecki, G., Łecki, M., Gutkowski, A. N., Andrzejewski, D., Warwas, B., Kowalczyk, M., Romaniak, A. (2021). Experimental and numerical study of heat pipe heat exchanger with individually finned heat pipes. *Energies*, 14(17). <https://doi.org/10.3390/en14175317>
 38. Council of European Union (2014). Supplementing directive 2010/30/ eu of the european parliament and of the council with regard to energy labelling of residential ventilation units (OJ L 337, 25.11.2014). <http://data.europa.eu/eli/regdel/2014/1254/oj>
 39. ANSYS(R) Academic Research CFD, Release 19.1, Help System. Fluent Theory Guide. ANSYS, Inc.
 40. Menter, F., Langtry, R., Völker, S., Huang, P. (2005). Transition modelling for general purpose CFD codes (pp. 31–48). <https://doi.org/10.1016/B978-008044544-1/50003-0>
 41. Bahiraei, M., & Mazaheri, N. (2021). A comprehensive analysis for second law attributes of spiral heat exchanger operating with nanofluid using two-phase mixture model: Exergy destruction minimization attitude. *Advanced Powder Technology*, 32, 211–224. <https://doi.org/10.1016/j.japt.2020.12.005>
 42. Gholamalizadeh, E., Hosseini, E., Jamnani, M. B., Amiri, A., saee, A. D., & Alimoradi, A. (2019). Study of intensification of the heat transfer in helically coiled tube heat exchangers via coiled wire inserts. *International Journal of Thermal Sciences*. <https://doi.org/10.1016/j.ijthermalsci.2019.03.029>
 43. Pal, E., Kumar, I., Joshi, J. B., & Maheshwari, N. K. (2016). Cfd simulations of shell-side flow in a shell-and-tube type heat exchanger with and without baffles. *Chemical Engineering Science*, 143, 314–340. <https://doi.org/10.1016/j.ces.2016.01.011>
 44. Menter, F. R., Langtry, R., Likki, S., Suzen, Y. B., Huang, P. G., Völker, S. (2006). A correlation-based transition model using local variables—part i: Model formulation. *ASME: Journal of Turbomachinery*, 128, 413–422. <https://doi.org/10.1115/1.2184352>
 45. Menter, F. R. (1994). Two-equation eddy-viscosity turbulence models for engineering applications. *AIAA Journal*, 32, 1598–1605. <https://doi.org/10.2514/3.12149>
 46. Rezaeiha, A., Montazeri, H. H., & Blocken, B. (2019). On the accuracy of turbulence models for cfd simulations of vertical axis wind turbines. *Energy*. <https://doi.org/10.1016/j.energy.2019.05.053>

47. Peng, D.-Y., & Robinson, D. B. (1976). A new two-constant equation of state. *Industrial & Engineering Chemistry Fundamentals*, 15(1), 59–64. <https://doi.org/10.1021/i160057a011>
48. Caillou, S. & Van den Bossche, P. (2012). Heat recovery efficiency: Measurement and calculation methods. In *The 33rd AIVC and 2nd TightVent Conference*. Air Infiltration and Ventilation Centre (AIVC), Ghent. <https://www.aivc.org/resource/heat-recovery-efficiency-measurement-and-calculation-methods>
49. El Maakoul, A., Laknizi, A., Saadeddine, S., Ben Abdellah, A., Meziane, M., & El Metoui, M. (2017). Numerical design and investigation of heat transfer enhancement and performance for an annulus with continuous helical baffles in a double-pipe heat exchanger. *Energy Conversion and Management*, 133, 76–86. <https://doi.org/10.1016/j.enconman.2016.12.002>
50. Saudia Basic Industries Corporation (SABIC) (2020). Lnptm konduittm compound ox11315. <https://www.sabic.com/en/products/specialties/lnp-compounds-and-pc-copolymer-resins/lnp-konduit-compound>
51. Roache, P. J. (1997). Quantification of uncertainty in computational fluid dynamics. *Annual Review of Fluid Mechanics*, 29(1), 123–160. <https://doi.org/10.1146/annurev.fluid.29.1.123>. Accessed 27 Dec 2023
52. Roache, P. J. (1994). Perspective: A method for uniform reporting of grid refinement studies. *Journal of Fluids Engineering*, 116(3), 405–413. <https://doi.org/10.1115/1.2910291>
53. Franke, J. & Frank, W. (2008). Application of generalized richardson extrapolation to the computation of the flow across an asymmetric street intersection. *Journal of Wind Engineering and Industrial Aerodynamics*, 96(10):1616–1628. 4th International Symposium on Computational Wind Engineering (CWE2006). <https://doi.org/10.1016/j.jweia.2008.02.003>
54. Stern, F., Wilson, R. V., Coleman, H. W., & Paterson, E. G. (2001). Comprehensive approach to verification and validation of CFD simulations-Part 1: Methodology and procedures. *Journal of Fluids Engineering*, 123(4), 793–802. <https://doi.org/10.1115/1.1412235>

Publisher's Note

Springer Nature remains neutral with regard to jurisdictional claims in published maps and institutional affiliations.